Microfluidics and Nanofluidics (2018) 22:137
https://doi.org/10.1007/s10404-018-2160-3

RESEARCH PAPER

Vortex-free high-Reynolds deterministic lateral displacement (DLD) via airfoil pillars

Brian M. Dincau[1] · Arian Aghilinejad[1] · Xiaolin Chen[1] · Se Youn Moon[1,2] · Jong-Hoon Kim[1]

Received: 25 June 2018 / Accepted: 8 November 2018

Abstract
One essential step in biosample analysis is the purification, separation, or fractionation of a biofluid prior to transport to the biosensor. Deterministic lateral displacement (DLD) has demonstrated the potential for continuous size-based separation of numerous medically relevant particles and organisms, such as circulating tumor cells, red blood cells, and even viral particles. Recently, high-throughput DLD separation has been demonstrated by utilizing higher flow rates, but this also results in changing separation dynamics as the Reynolds number (*Re*) increases. It has been observed that the critical diameter (D_c) for a DLD device decreases as *Re* climbs, and theorized that both streamline compression and vortex emergence may contribute to this phenomenon. The precise mechanism for this shift has been difficult to isolate, however, due to the coupled nature of vortex emergence and streamline compression in high-*Re* DLD devices with circular pillars. To decouple these effects, we have characterized the performance of a DLD device with symmetric airfoil pillars that do not produce vortices up to $Re = 100$. In demonstrating a complete particle trajectory shift at $Re = 51$, we have shown that vortex effects are not a predominant contributor to this D_c shift, thus streamline evolution is likely to be the primary mechanism. Furthermore, we have compared the performance of this device to a similar device with rotated pillars having a negative 15° angle of attack, and found that separation effectiveness declines as streamlines become highly asymmetric and small particles exhibit significant variation in their trajectories.

Keywords Separation and purification · High throughput · Deterministic lateral displacement · High Reynolds · Microvortices

1 Introduction

Biosample preparation is a crucial step in biomedical analysis, typically preceding transport of the sample to the biosensor. Preparation often involves the concentration or fractionation of a sample, to amplify the sensor response. While numerous active concentration techniques (Aghilinejad et al. 2018; Yeo et al. 2013; Dincau et al. 2017a, b) are being developed, passive techniques are more desirable for improved scalability and simpler microscale integration. Passive size-based particle separation by deterministic lateral displacement (DLD) has demonstrated significant biomedical applications, such as the fractionation of whole blood (Zheng et al. 2005; Inglis et al. 2011) and the concentration of target analytes such as circulating tumor cells (Loutherback et al. 2012) or even DNA (Chen et al. 2015). DLD devices utilize hydrodynamic forces to passively separate particles as they flow through an array of pillars (Huang et al. 2004; Inglis et al. 2006), with a demonstrated potential for faster processing speeds and significantly reduced cost when compared to conventional separation techniques such as centrifugation or microfiltration (Dincau et al. 2017a, b). Historically, DLD devices have been limited in throughput due to relatively low flow rates, often reported in µL/min or mL/hr. To improve this throughput, DLD performance has been studied with higher flow rates, resulting in a proportionate rise in the Reynolds number (*Re*). This means that

Electronic supplementary material The online version of this article (https://doi.org/10.1007/s10404-018-2160-3) contains supplementary material, which is available to authorized users.

✉ Jong-Hoon Kim
jh.kim@wsu.edu

[1] School of Engineering and Computer Science, Washington State University, Vancouver, WA 98686, USA

[2] Department of Quantum System Engineering, Chonbuk National University, 567 Baekje-daero, Jeonju, Jeollabuk-do 54896, Republic of Korea

Published online: 14 November 2018

inertial effects become more significant for high-throughput DLD devices, thus separation characteristics may deviate from traditional low-*Re* ($Re < 1$) devices (Di Carlo 2009).

It has been demonstrated that the critical diameter (D_c), a dimension that describes the minimum particle size that can be separated in a DLD array, is actually a dynamic property that decreases with increasing *Re* at both the macroscale (Lubbersen et al. 2012, 2013) and microscale (Dincau et al. 2017, 2018). It has been theorized that streamline compression and vortex development with increasing *Re* are both contributors to this shift (Lubbersen et al. 2013; Dincau et al. 2018; Kim et al. 2017). Streamline compression may cause a D_c shift by altering the drag forces encountered by particles along their trajectory. As illustrated in Fig. 1(a), sufficiently large streamlines can fully envelop the particle at low *Re*, dominating its trajectory and resulting in a zig-zag mode. Figure 1b illustrates how thinner streamlines at higher *Re* are no longer wide enough to completely envelop the same particle. In this case, the particle is influenced by drag forces from multiple streamlines, resulting in a bumped mode that follows the tilt angle. This compression has been verified numerically as demonstrated in Fig. 1c. It has also been shown that decreasing the vertical gap size in a DLD array can decrease the critical diameter (Zeming et al. 2016). Similarly, vortex development may functionally reduce the vertical gap size under high-*Re* conditions as the stagnation zones begin to choke the vertical gaps (Lubbersen et al. 2013; Dincau et al. 2018). However, it has been challenging to separate the effects of streamline evolution and vortex growth under high-*Re* conditions until recently. This is due, in part, to the inseparable coupling of high-*Re* streamline effects and vortex effects in a traditional DLD device with circular pillars. We encountered this in our previous study of high-*Re* flow through a circular DLD array, wherein microvortices would emerge at moderate Reynolds numbers ($Re \approx 25$) and grow as *Re* increased. This made it impossible to distinguish vortex effects from streamline effects with respect to overall device performance (Dincau et al. 2018). To shed light on the relative contributions of streamline compression and vortex development, we have investigated DLD performance with a device utilizing symmetric airfoil pillars with a neutral angle of attack (AoA) to decouple the vortex and streamline effects. While Al-Fandi et al. have numerically investigated an asymmetric airfoil DLD for enhanced separation, their study was limited to low-*Re* flow (Al-Fandi et al. 2011). Therefore, this is the first study that we know of to investigate high-*Re* DLD performance with airfoil pillars.

Through numerical simulation of flow fields, we have shown that this pillar geometry does not develop vortices in their wake, even up to $Re = 100$. Therefore, any changes in D_c should be attributed to streamline evolution, as illustrated in Fig. 1, rather than vortex emergence. To better understand the influence of vortices, we have also investigated a nearly identical device with the same pillar and array dimensions, but rotated the pillars such that they have a negative 15° AoA relative to the bulk flow direction. This configuration yields significant vortices, which emerge around $Re = 45$. By characterizing the performance of these two devices, we have shown that the D_c shift is primarily a result of streamline

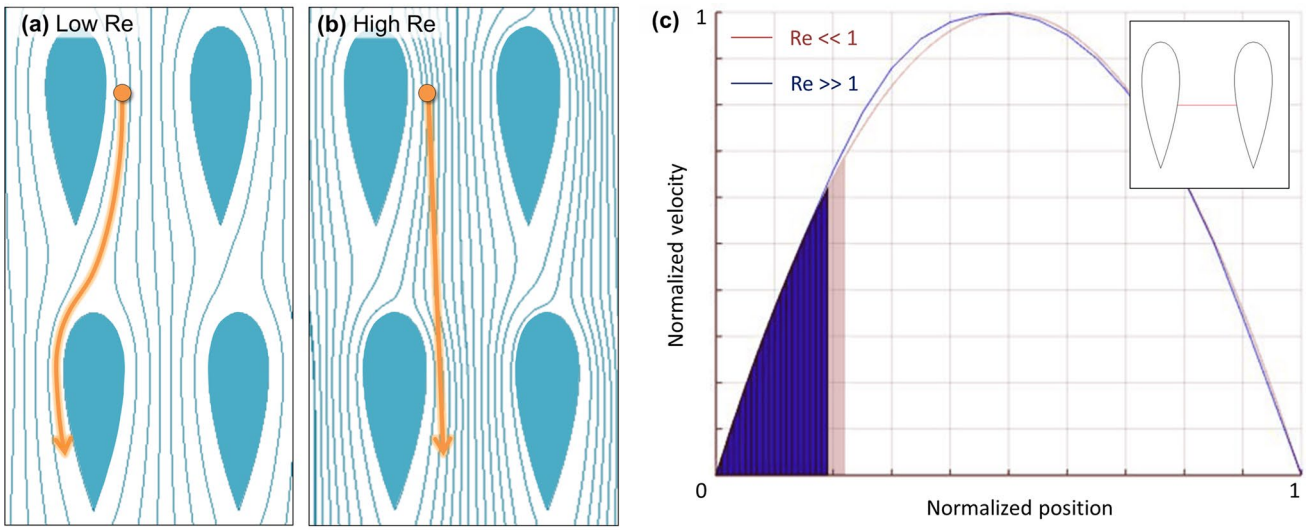

Fig. 1 Illustration depicting the effect of streamline compression on particle trajectory. From general DLD theory: **a** at low *Re*, individual streamlines are large enough to envelop the target particle, inducing a zig-zag trajectory through the array. **b** At high *Re*, streamline compression allows the particle to be influenced by multiple streamlines simultaneously. This averaging effect results in a bumped mode through the array. **c** A numerically generated plot showing the reduction in a single streamline width with increasing *Re*. The velocity profile between two pillars is plotted on the curve, while the shaded region represents the width of the first streamline near the pillar wall

compression, rather than vortex effects. Furthermore, we note that the high degree of asymmetry in streamlines for the AoA configuration, which eventually results in vortex emergence, is also associated with a particle spreading phenomenon which may decrease functional separation resolution. Thus vortex mitigation and streamline symmetry may be essential criteria for high-throughput DLD design.

2 Methods

2.1 Numerical methods

The initial 2D flow fields for various pillar shapes and orientations were modeled in COMSOL Multiphysics, a finite-element-based software package. The airfoil chosen for both the numerical and experimental investigations was based on a modified NACA0030, a standardized code used to denote the relative airfoil dimensions. The 00 indicates that there is no camber (hence symmetric), while the 30 indicates a 30% thickness-to-chord ratio. The pillars were scaled by a factor of 90, resulting in airfoils approximately 90 µm in length and 30 µm in maximum thickness. After establishing the relevant 2D geometries in COMSOL, a constant flow velocity was defined at the inlet, and the outlet was fixed at atmospheric pressure with no-slip conditions defined at all other boundaries. The flow field simulations were run up to $Re = 100$, and the working fluid was defined to be water. With geometries and boundary conditions prescribed, the Navier–Stokes and continuity equations were solved to obtain the velocity flow fields. With the flow field model established, particle trajectories were then investigated using a particle tracing model, which predicts particle movement based on drag forces. Simulated particles of varying size were injected at a fixed position, and their trajectories were observed through the airfoil arrays. In this approach, simulated particles were transported by hydrodynamic forces through a DLD array containing hundreds of airfoil-shaped microposts. This allowed us to ignore the flow asymmetries imparted at the inlet, outlet, and device sidewalls, thus providing a more realistic insight for the much-longer experimental device.

2.2 Fabrication techniques

Both device configurations were fabricated using traditional soft lithography techniques. Photolithography was used to pattern a negative SU-8 3050 master mold on a 4 in. silicon wafer, which was used to fabricate several devices via polydimethylsiloxane (PDMS) casting. PDMS devices were sealed against a glass slide by oxygen plasma bonding. Additional fabrication considerations, such as substrate preparation and thermal ramping, are detailed in our previous work (Dincau et al. 2018). Finally, to mitigate polystyrene particle trapping in the experimental devices, a 3-h surface treatment of 2 mM sodium dodecyl sulfate (SDS) in deionized (DI) water was applied immediately after plasma bonding. (Garcia et al. 2005; Roman et al. 2006; Zhou et al. 2010).

2.3 Experimental methods

The experimental setup utilized an array of syringe pumps (kdScientific KDS-200, New Era NE-1000X) to drive the buffer and sample injection. Once the desired flow rate was achieved and all bubbles evacuated from the array, polystyrene microparticles (Thermos Scientific, Sigma-Aldrich, Phosphorex, Max Std Dev < 2% of nominal size) were injected through the sample inlet, as illustrated in Fig. 2. Particle trajectories were recorded using a high-speed camera (Phantom Mira 310) mounted on an optical microscope (Nikon Eclipse Ci). Recordings were typically captured at ~ 11,000 frames per second to ensure frame-to-frame particle traceability. Particle trajectories were characterized

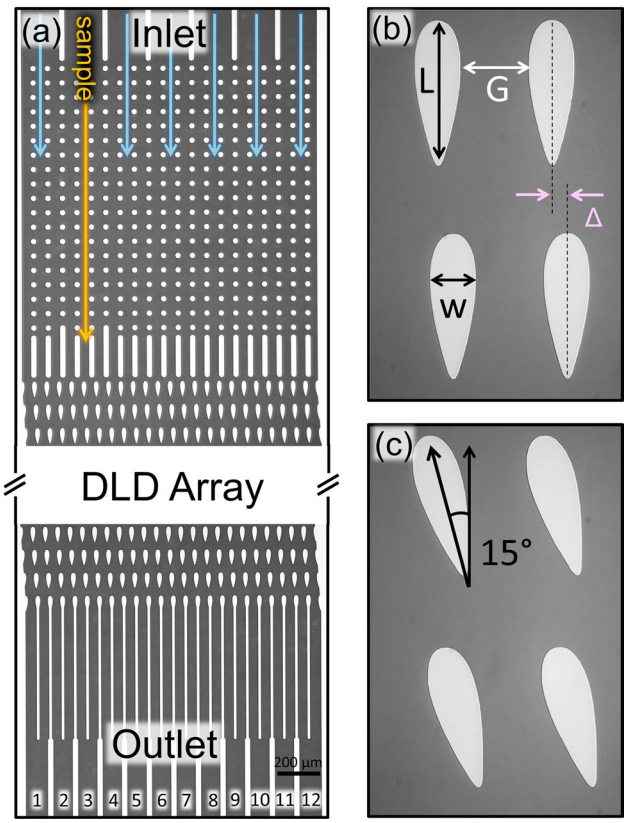

Fig. 2 Representative photomask images of the airfoil DLD device. **a** The sample pathway is shown in orange, with buffer pathways shown in light blue. Outlet channels are numbered from left to right, with 1–4 corresponding to a pure zig-zag trajectory and 9–12 a bumped trajectory. **b** A closer view of the neutral airfoil array where $L = 85$ µm, $w = 27$ µm, $G = 40$ µm, and $\Delta = 8.4$ µm. These devices had a constant depth of approximately 180 µm. **c** A closer view of the AoA array with rotation angle indicated

based on particle distributions at the outlet, where the low-numbered outlets (1–4) correspond to the zig-zag mode and high-numbered outlets (9–12) correspond to the bumped mode, as labeled in Fig. 2. Note that for these arrays, we have used a sidewall-compensating technique, in which the sidewalls of the device periodically shift with the array, thus preserving row-to-row flow symmetry without altering the overall array centerline. This improves flow dynamics near the sidewalls and significantly reduces particle clogging. This technique was also used in a DLD array designed by Inglis et al. in 2011 (Inglis et al. 2011) for high-throughput enrichment of leukocytes. A more comprehensive view of our mask design can be seen in Supplementary Figure S.1.

3 Results and discussion

3.1 Numerical results

The simulated streamline patterns for both pillar configurations are shown in Fig. 3. Here, we can clearly see that the pillars with no angle of attack do not develop vortices up to $Re = 100$. Therefore, any significant changes in device performance within this Reynolds range should be attributed to streamline evolution or other non-vortex effects. On the other hand, the negative 15° AoA pillars develop significant vortices by $Re = 67$ with strong vortex pairs at $Re = 100$. They also exhibit a greater degree of asymmetry, especially in the crossover regions between pillars. Through iterative calculations at different flow rates, this simulation predicts the onset of vortices around $Re = 45$ in the negative AoA case. We have also simulated a positive AoA case and observed similar vortex development, but decided to proceed experimentally with only the neutral and negative configurations. This is because our numerical model predicts a lower pressure drop in the negative AoA configuration than in the positive. We sought to minimize pressure drop to investigate the highest *Re* regime that our experimental setup could achieve, thus selected the negative AoA configuration for experimental validation. Additional numerical results for the positive AoA configuration, as well as nominal pressure drop estimates, can be viewed in our supplementary information. (Supplementary Figure S.2, S.3, and S.4).

With the flow fields established, we then numerically injected several sizes of particles (9–20 μm with 0.5-μm increments) and classified their trajectories over a range of Reynolds numbers, to gather a general sense of device performance. The results of this analysis are plotted in Fig. 4, which predicts separation performance up to $Re \approx 50$. In these plots, we have non-dimensionalized the particle size (D_p) as a ratio over the initial critical diameter ($D_{c,i}$), allowing for a more direct comparison of the two configurations. $D_{c,i}$ was iteratively determined by running our simulation for the previously mentioned range of particle sizes in a low-*Re* regime ($Re = 0.7$), and observing the threshold particle size at which a fully bumped mode is observed. We then continued to investigate the trajectories for all particle sizes at five different increasing Reynolds numbers ($Re = 7$, 17.5, 28, 35, and 48). For each Reynolds number, the trajectory for each particle was classified as either zig-zag, mixed, or bumped, yielding the distributions shown in Fig. 4. In both cases, we observe a decrease in the critical diameter with increasing *Re*, as shown in previous high-*Re* DLD investigations (Lubbersen et al. 2012, 2013; Dincau et al. 2018). The most notable difference in these two configurations is the size of the region between zig-zag and bumped trajectories. Particles with diameters within this region do not follow a purely bumped or purely zig-zag trajectory at the corresponding *Re*; thus we have labeled it a mixed mode in the figure. We note that this wide mixed region for the AoA device occurs at all *Re* values, not just at values where vortices are developed. Therefore, we do not attribute this phenomenon to vortex effects. Rather, the streamlines in the AoA device exhibit much steeper curvatures with greater asymmetry to navigate the rotated pillars. This manifests as a stronger net lateral velocity in each unit cell, as described by Kim et al. (2017), who demonstrated that the anisotropic permeability of row-shifted parallelogram DLD layouts results in a nonzero migration angle for some particles smaller than D_c. They define this trajectory as an altered zig-zag mode,

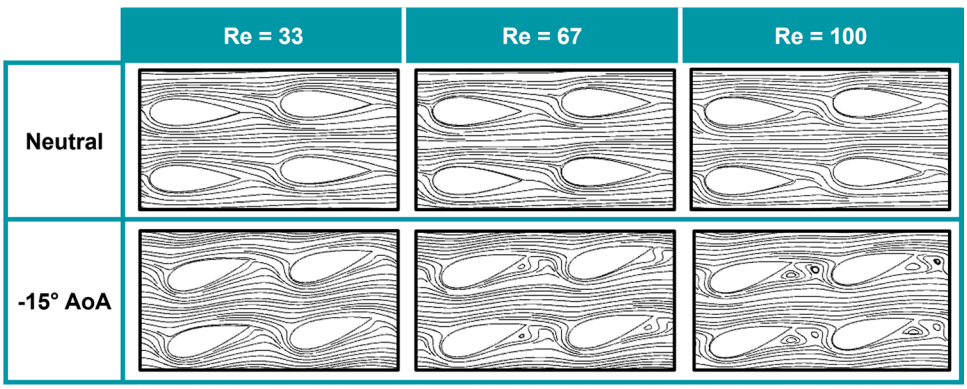

Fig. 3 Numerically generated streamlines showing the absence of vortices for a DLD device with neutral airfoil pillars (top) and significant vortex development for the negative 15° configuration (bottom) with increasing *Re*. Also note the steeper lateral component of the AoA streamlines, especially in the crossover regions between pillars

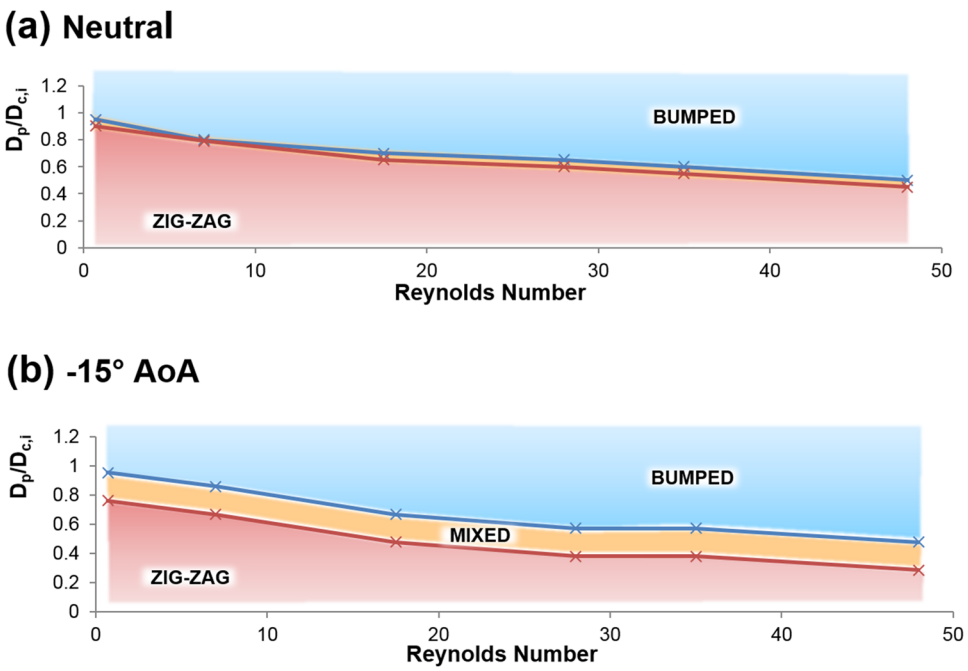

Fig. 4 Comparison of the D_c shift for two different airfoil pillar configurations. The particle size $\boldsymbol{D_p}$ has been non-dimensionalized as a ratio over the initial critical diameter $D_{c,i}$. **a** The neutral configuration yields clear zig-zag and bumped modes, with a very thin transition region. **b** The negative AoA configuration yields a wider transition region. Both configurations predict a similarly decreasing D_c with increasing *Re*

and approximate the migration angle as the angle between the average velocity vector and the pressure gradient direction for a given unit cell. The mixed mode region is much narrower for the neutral configuration, perhaps because the lateral velocity component is significantly reduced and does not change much with increasing *Re*.

3.2 Experimental results

Through preliminary flow testing, the neutral and AoA devices were estimated to possess an initial D_c of approximately 25 µm and 22 µm, respectively. This estimation was limited by the size resolution of available microparticles. For the neutral device, we witnessed 20-µm particles follow a complete zig-zag mode and 30-µm particles follow a complete bumped mode at low *Re*. Thus, we approximate $D_{c,i}$ as the value between these two. In the AoA device, we witnessed 20-µm particles follow a mixed mode, rather than complete zig-zag, while still visualizing a complete bumped mode for the 30-µm particles. Due to the mixed trajectory, we classified $D_{c,i}$ for the AoA device as slightly smaller than the neutral device, but larger than 20 µm. To investigate the transition region for these devices, particles sizes well below the initial D_c were chosen. Figure 5 summarizes the trajectory distributions for 20-µm particles in the neutral device and 15-µm particles in the AoA device

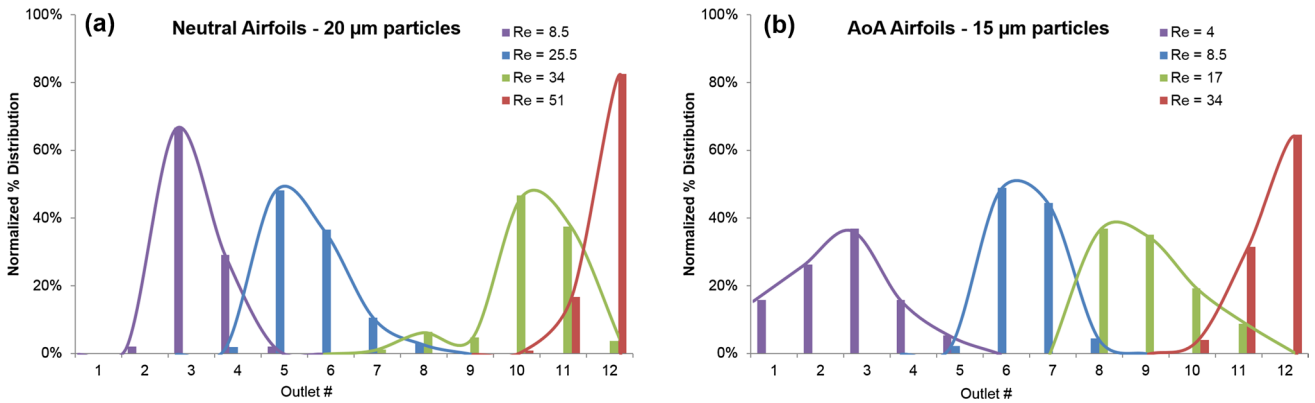

Fig. 5 Experimental demonstration of the Dc shift for both device configurations with increasing *Re*. The shift appears similar for both configurations for particle sizes near $D_{c,i}$. **a** The neutral configuration yields a sharp transition from zig-zag to bumped, as indicated by the significant distribution change from $Re = 25.5$ to $Re = 34$. The AoA configuration yielded a more gradual transition from zig-zag to bumped

over a similar Reynolds range. These distributions were obtained by reviewing individual frames of the high-speed video. Particles were counted as they passed through each outlet (1–12) over the duration of the recording. For each combination of flow rate and particle size, at least 50 continuous particles were tracked, with most recordings capturing upwards of 150 particles. For instance, 189 continuous particles were tracked to create the distribution curve for 20-μm particles at $Re = 34$ in the neutral device. Since the precise number of particles varied between recordings, the curves have been normalized for direct comparison. In these plots, and as noted in Fig. 2, the low-numbered outlet channels (1–4) correspond to the zig-zag mode, while the high-numbered channels (9–12) correspond to the bumped mode. Thus, the region in between can be classified as mixed or altered zig-zag. For both experimental devices, a D_c shift was observed with increasing *Re*, similar to that of our previous study. Therefore, it is quite evident that the D_c shift is a result of streamline compression, rather than vortex effects, because the neutral device exhibited the same shift as previously noted despite a complete lack of vortices.

In this study, we aimed to compare the transition region for both devices to relate our experimental observations to our numerical prediction. These occurred at slightly different *Re* values in each device, due to differences in both particle size and streamline dynamics. The greatest difference between these two distribution plots is the relative length of this transition region. The location of the distribution peak for 20-μm particles in the neutral device changed drastically from $Re = 25.5$ to $Re = 34$, moving from outlet 5 to outlet 10. In other words, with only a 33% relative increase in *Re*, we observed a five-lane shift in the location of the distribution peak. This was not the case for the AoA device; instead the transition from zig-zag to bumped was more gradual, requiring a relatively greater change in *Re* to experience the full shift. For example, from $Re = 8.5$ to $Re = 17$, we note a 100% increase in *Re* with only a two-lane shift in the location of the distribution peak. Overall, these results demonstrate a narrower transition region for the neutral device and a wider transition region for the AoA device, agreeing with our numerical predictions. We also note that the distributions corresponding to lowest *Re* and highest *Re* for the neutral device are sharper than in the AoA device, with peak magnitudes of 67% and 83%, respectively, versus 37% and 65% in the AoA device. This spreading effect is discussed in greater detail at the end of this section.

With the transition period investigated, we aimed to characterize the mixed sample separation performance of these two devices, utilizing the *Re*-induced D_c shift to fractionate a sample containing 10-, 15-, and 20-μm particles. These results are plotted in Fig. 6. For this set of figures, we present the initial low-*Re* distribution to show that all particles follow a zig-zag mode initially, thus could not be separated under low-*Re* conditions as shown in Fig. 6a, b. We also present the high-*Re* operating condition, when the overlap between particles of different size was minimized. While both device configurations could easily separate 100% of the 20-μm particles with a sufficient *Re*, only the neutral configuration could effectively fractionate the entire sample. Assuming independent collection for all 12 outlets, the neutral configuration was able to effectively separate 75% of the total 10-μm particles (outlet 1–4) and 83% of the total 15-μm particles (outlets 5–8) at $Re = 42.5$ (Fig. 6c). However, the best conditions that we could achieve at in the AoA configuration, $Re = 25.5$, yielded only 24% (outlets 1–7) and 63% (outlets 8–10), respectively (Fig. 6d). If purification is desired over concentration or fractionation, we also present a purification-focused collection scheme for the neutral device in supplementary Figure S.5. We believe that the performance of the neutral device could be further improved in several ways. The simplest improvement would be to run the device at a higher flow rate. Based on the observed trend, a more complete fractionation may have been achieved at a higher Reynolds value, but we were unable to achieve this due to experimental limitations. Fabricating the devices with a more rigid substrate, such as glass or silicon, would allow them to withstand greater internal pressures. Additionally, by utilizing the device in a recirculating loop configuration, the sample could be iteratively purified. This would allow for adjustment of *Re* as the sample approaches higher purity to more precisely control D_c. Finally, increasing the overall width of the DLD array and including additional collection outlets may allow for a greater degree of particle differentiation and a more precise collection scheme.

Qualitatively, the reason for poor fractionation performance in the AoA configuration stems from the wide distributions of the 15 μm and especially the 10-μm particles. While it was possible to reduce the 15 μm spreading by increasing *Re*, as demonstrated in Fig. 5b at $Re = 34$, this resulted in complete overlap with the 20-μm particles. This spreading effect, which is further plotted for the 10-μm particles in supplementary Figure S.6, shows a strong correlation with increasing *Re*. Initially, this was thought to be a sort of chaotic mixing resulting from the emergence of microvortices in the array. However, this cannot be the case, because vortices do not emerge in the AoA configuration until about $Re = 45$, yet the spreading becomes apparent for the 10-μm particles as soon as $Re = 8.5$. At the same time, the 15- and 20-μm particles generally did not exhibit the same degree of spreading in either device at any of the tested *Re* values. Thus we have a breakdown in typical DLD operation, in which the 10-μm particles do not follow a few deterministic paths. Rather, they exhibit a high degree of variation in their trajectories with increasing *Re*. Kulrattanarak et al. (2011) have also noticed this irregular particle spreading, and theorized that particles traveling near the stagnation

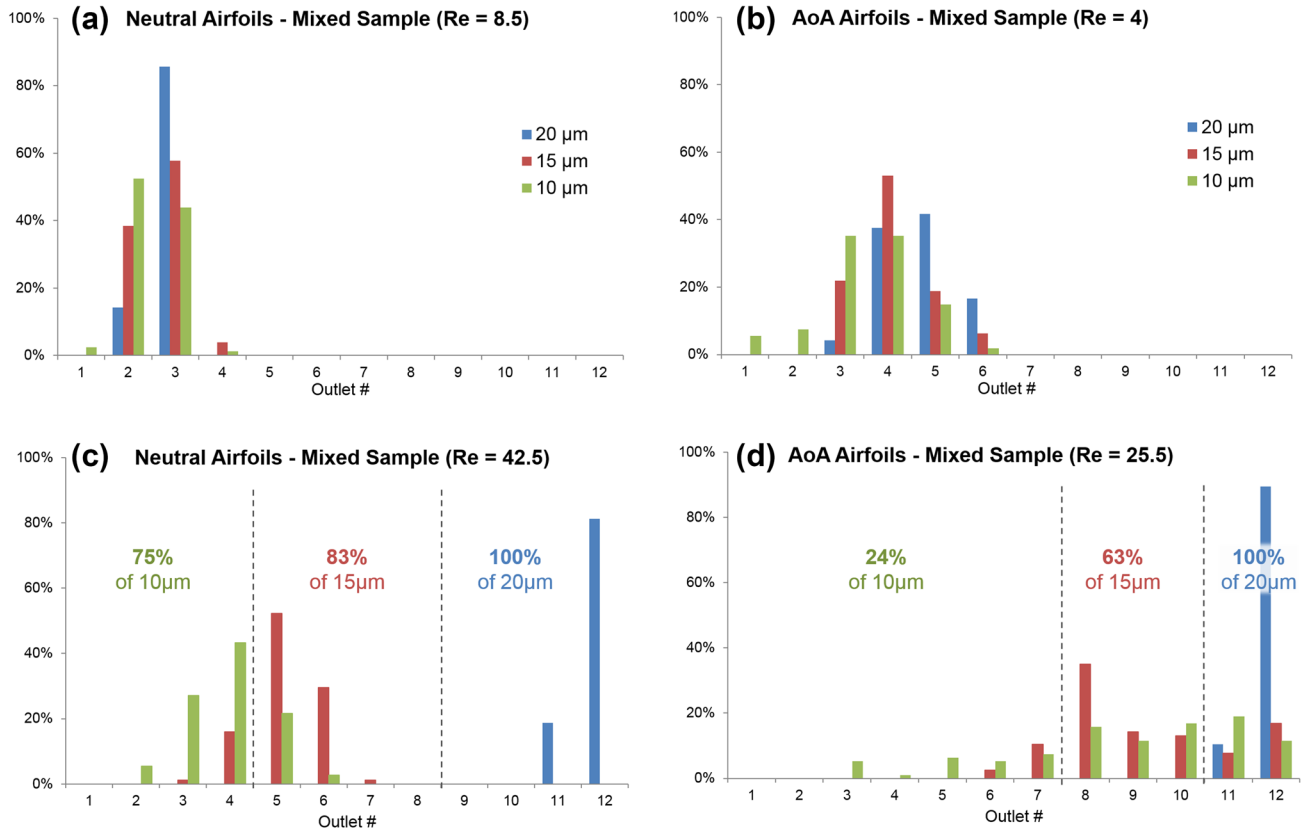

Fig. 6 Summary of the experimental results for mixed sample fractionation. The vertical axis denotes normalized % distribution for particles of a given size, as in the previous figure. **a, b** At the low-*Re* operating condition, all particle sizes follow a predominantly zigzag mode. **c** At the high-***Re*** operating condition, the neutral device could effectively fractionate 75% of the 10-µm particles, 83% of the 15-µm particles, and 100% of the 20-µm particles. **d** At the high-***Re*** operating condition, the AoA device could effectively fractionate 24% of the 10-µm particles, 63% of the 15-µm particles, and 100% of the 20-µm particles

points behind pillars may be more susceptible to Brownian motion and colloidal forces. While it is unlikely that Brownian motion issignificant for 10-µm particles at these *Re* values, an increased susceptibility to colloidal forces is still possible. Generally, only particles smaller than D_c encounter these stagnation points, while particles larger than D_c maintain a much higher average velocity as they bump through the array. Thus particles larger than D_c would not experience the same colloidal susceptibility as particles smaller than D_c. Still, colloidal forces may not justify the magnitude of spreading observed in the AoA device, as the particle concentration used for these experiments was approximately 0.1% (solids).

The most likely contributor to this spreading effect may be the anisotropy that develops in the AoA device at higher flow rates. When comparing the forward and lateral velocities of our simulated array, the neutral device is largely dominated by forward flow with anisotropies less 0.1% up to $Re = 48$. However, the AoA device develops some anisotropy, between 1 and 2% at $Re = 48$. This indicates that the D_c shift is largely a product of streamline compression in the neutral device, while both streamline compression and growing anisotropy contribute to the greater shift witnessed in the AoA device. One undesirable effect of this lateral flow is a departure from pure DLD flow, in which all particles are pushed in the direction of anisotropy, hindering device performance at higher flow rates as exemplified in Fig. 6d. This anisotropy or asymmetry has been more thoroughly investigated by previous studies (Kim et al. 2017; Kulrattanarak et al. 2011) and should be mitigated to prevent a breakdown in performance under high-*Re* conditions.

Another possible explanation for these chaotic trajectories may be the development of three-dimensional flow in the wake of the pillars. To investigate this possibility, we have simulated three-dimensional (3D) streamlines in a representative 3×3 pillar array, for both the neutral and AoA configurations (See supplementary Figure S.7). Here, we note the presence of 3D vortices in the wake of the pillars at $Re \approx 40$, with velocity magnitudes of up to 10% of the bulk flow. Furthermore, the AoA configuration yields larger vortices with greater variation in velocity. Particles with trajectories that pass near the crossover regions between pillars

may experience a similar 3D velocity profile, allowing them to occasionally circulate and switch flow lanes where 2D flow would not predict. This effect is most pronounced in the AoA case, as highlighted in supplementary Figure S.8, due to the increased number of streamlines intersecting with these regions. On the other hand, larger particles that tend to follow a predominantly bumped mode take a much straighter path, thus they may not experience the same 3D flow regions as smaller particles. This spreading phenomenon was not observed in the neutral configuration, perhaps because streamlines are able to navigate the neutral airfoil pillars without the drastic asymmetry observed in the AoA configuration and without frequent intersection with the 3D flow regions. Thus, flow lane symmetry, with respect to both 2D anisotropy and 3D vortex formation, is essential design criteria for efficient high-*Re* DLD devices.

4 Conclusion

DLD has demonstrated the potential for wide-scale use in biosample preparation, particularly in applications requiring continuous passive size-based particle separation. To meet the demand for high-throughput operation, high flow rates must be utilized, resulting in a higher Reynolds regime. Previously, it has been observed that D_c decreases with increasing *Re*. The primary mechanism for this shift has been difficult to isolate, due to the fact that both streamline compression and vortex emergence go hand-in-hand with increasing *Re* in traditional DLD devices with circular pillars. In this investigation, we have decoupled streamline and vortex effects by utilizing pillars with a symmetric airfoil shape, which do not produce vortices under high-*Re* operating conditions. We have demonstrated a complete shift in particle trajectories through this airfoil device, both numerically and experimentally, thus we conclude that the D_c shift is not a result of vortex emergence, but rather a combination of two other phenomena. Streamline compression appears to be the primary mechanism for reducing D_c in the neutral device, while growing anisotropy results in a stronger apparent shift in the AoA device. By comparing the performance characteristics of a device with neutrally oriented pillars to another device with negative 15° AoA pillars, we have also shown that separation quality diminishes as lateral flow ($> 1\%$) and asymmetric 3D flow patterns emerge at higher flow rates in the AoA configuration. Overall, this study has shown that high-*Re* DLD design requires significant consideration for pillar shape and orientation, to control streamline symmetry and vortex emergence. It has also shown that three-dimensional flow may be significant in high-throughput DLD devices, and would be worthy of further characterization to obtain a more comprehensive understanding of DLD mechanics. For now, DLD devices having symmetric airfoil pillars with no AoA may serve as an excellent starting point for high-throughput design, due to their mitigation of vortex effects and preservation of flow symmetry under high-*Re* conditions.

Acknowledgements JK and BD acknowledge partial financial support from the Washington State University New Faculty Seed Grant (131078) and the National Science Foundation (NSF CBET-1707056).

Conflict of interest The authors declare no conflicts of interest related to the presented work.

References

Aghilinejad A, Aghaamoo M, Chen XL, Xu J (2018) Effects of electrothermal vortices on insulator-based dielectrophoresis for circulating tumor cell separation. Electrophoresis 39:869–877

Al-Fandi M, Al-Rousan M, Jaradat MAK, Al-Ebbini L (2011) New design for the separation of microorganisms using microfluidic deterministic lateral displacement. Robot Comput Integr Manuf 27:237–244

Chen Y, Abrams ES, Boles TC, Pedersen JN, Flyvbjerg H, Austin RH, Sturm JC (2015) Concentrating genomic length DNA in a microfabricated array. Phys Rev Lett 114:198303

Di Carlo D (2009) Inertial microfluidics. Lab Chip 9:3038–3046

Dincau BM, Lee Y, Kim JH, Yeo WH (2017a) Recent advances in nanoparticle concentration and their application in viral detection using integrated sensors. Sensors 17:2316

Dincau B, Aghilinejad A, Kim J-H, Chen X (2017b) Characterizing the high reynolds number regime for deterministic lateral displacement (dld) devices. In: ASME Internation Mechanical Engineering Congress and Exposition, vol 10. Micro- and Nano-Systems Engineering and Packaging, Tampa

Dincau BM, Aghilinejad A, Hammersley T, Chen X, Kim J-H (2018) Deterministic lateral displacement (dld) in the high reynolds number regime: High-throughput and dynamic separation characteristics. Microfluid Nanofluid 22:59

Garcia CD, Dressen BM, Henderson A, Henry CS (2005) Comparison of surfactants for dynamic surface modification of poly(dimethylsiloxane) microchips. Electrophoresis 26:703–709

Huang LR, Cox EC, Austin RH, Sturm JC (2004) Continuous particle separation through deterministic lateral displacement. Science 304:987–990

Inglis DW, Davis JA, Austin RH, Sturm JC (2006) Critical particle size for fractionation by deterministic lateral displacement. Lab Chip 6:655–658

Inglis DW, Lord M, Nordon RE Scaling deterministic lateral displacement arrays for high throughput and dilution-free enrichment of leukocytes. J Micromech Microeng 2011, *21*

Kim SC, Wunsch BH, Hu H, Smith JT, Austin RH, Stolovitzky G (2017) Broken flow symmetry explains the dynamics of small particles in deterministic lateral displacement arrays. Proc Natl Acad Sci USA 114:E5034–E5041

Kulrattanarak T, van der Sman RGM, Lubbersen YS, Schroen C, Pham HTM, Sarro PM, Boom RM (2011a) Mixed motion in deterministic ratchets due to anisotropic permeability. J Colloid Interface Sci 354:7–14

Kulrattanarak T, van der Sman RGM, Schroen C, Boom RM (2011b) Analysis of mixed motion in deterministic ratchets via experiment and particle simulation. Microfluid Nanofluid 10:843–853

Loutherback K, D'Silva J, Liu LY, Wu A, Austin RH, Sturm JC Deterministic separation of cancer cells from blood at 10 ml/min. AIP Adv 2012, *2*

Lubbersen YS, Schutyser MAI, Boom RM (2012) Suspension separation with deterministic ratchets at moderate reynolds numbers. Chem Eng Sci 73:314–320

Lubbersen YS, Dijkshoorn JP, Schutyser MAI, Boom RM (2013) Visualization of inertial flow in deterministic ratchets. Sep Purif Technol 109:33–39

Roman GT, McDaniel K, Culbertson CT (2006) High efficiency micellar electrokinetic chromatography of hydrophobic analytes on poly(dimethylsiloxane) microchips. Analyst 131:194–201

Yeo WH, Lee HB, Kim JH, Lee KH, Chung JH Nanotip analysis for dielectrophoretic concentration of nanosized viral particles. Nanotechnology 2013, *24*

Zeming KK, Salafi T, Chen CH, Zhang Y Asymmetrical deterministic lateral displacement gaps for dual functions of enhanced separation and throughput of red blood cells. Sci Rep 2016, *6*

Zheng SY, Yung R, Tai YC, Kasdan H (2005) IEEE. In: Deterministic lateral displacement mems device for continuous blood cell separation, 18th IEEE International Conference on Micro Electro Mechanical Systems (MEMS). Miami Beach, pp 851–854 (**Jan 30–Feb 03**)

Zhou JW, Ellis AV, Voelcker NH (2010) Recent developments in pdms surface modification for microfluidic devices. Electrophoresis 31:2–16